


Boussinesq and non-Boussinesq turbulent plumes in a corner with applications to natural ventilation

Shuo Li * and M. R. Flynn

Department of Mechanical Engineering, University of Alberta, Edmonton, Alberta T6G 1H9, Canada



(Received 12 February 2021; accepted 4 May 2021; published 18 May 2021)

A previous formulation of plume merger [Rooney, *J. Fluid Mech.* **796**, 712 (2016)] is generalized to model both Boussinesq and non-Boussinesq plume rise in a corner of arbitrary angle $2\pi/n$ where $n \geq 1$. The Boussinesq plume theory predicts the correct near- and far-field similarity solutions when n is noninteger. Moreover, an alternate entrainment assumption is proposed whereby the rate of entrainment per unit height correlates directly to the plume perimeter. Model predictions made using this alternative entrainment assumption agree well with a previous prediction for the plume volume flux when $n = 2$. For non-Boussinesq plumes, the theory also approaches the correct near- and far-field similarity limits. When the source area is compact, and regardless of the corner angle, the non-Boussinesq height, i.e., height over which non-Boussinesq effects are important, is small compared to the contact height between the plume and the corner. When the source area is relatively large, the non-Boussinesq height can be comparable to the contact height; enhanced non-Boussinesq effects are observed for smaller corner angles. Our Boussinesq theory is adapted to the natural ventilation model developed by Linden *et al.* [*J. Fluid Mech.* **212**, 309 (1990)] and agrees well with previous experimental and theoretical predictions for the steady-state depth of the layer of discharged plume fluid that accumulates along the ceiling of the (ventilated) interior space. For non-Boussinesq plumes, the counterpart theory compares satisfactorily with previously measured results of fire plume mass flux.

DOI: [10.1103/PhysRevFluids.6.054503](https://doi.org/10.1103/PhysRevFluids.6.054503)

I. INTRODUCTION

The seminal work of Morton *et al.* [1] (MTT hereafter) modeled theoretically an isolated plume in an unbounded environment. In general, the MTT model consists of a set of three coupled ordinary differential equations representing the conservation of plume mass, momentum, and buoyancy; the set is closed by an entrainment assumption. On the basis of MTT, Baines and Turner [2] studied plume rise and discharge in a bounded environment, a composite flow referred to as a “filling box.” Over time, filling boxes lead to a stable ambient density stratification. The significance of Baines and Turner’s work in the architectural context was solidified by Linden *et al.* [3]. They considered plume rise in a ventilated filling box and thereby derived an estimate for the depth of the layer of discharged plume fluid that accumulates along the ceiling. A key finding from the work of Linden *et al.*, results from which have been adapted to the design of naturally ventilated buildings [4], is that the form of the ambient stratification that develops in the ventilated enclosure depends on the details of turbulent entrainment but not on the source buoyancy flux. The model of Linden *et al.* [3] has been extended in numerous follow-up studies, which have examined multiple noninteracting plumes [5], external wind forcing [6], transient effects [7], and ventilation of fires and non-Boussinesq plumes [8,9]. Where discrete plumes arise in the previous studies, they are assumed to be centrally situated so that

*shuo10@ualberta.ca

plume rise is not impeded by the presence of sidewall boundaries. When such an assumption cannot be justified, ambient entrainment into the rising plume is not axisymmetric leading to potentially significant deviations [10] from the dynamical descriptions provided by, e.g., MTT and Baines and Turner [2].

Insights into the importance of uniform versus nonuniform ambient entrainment are provided by studies devoted to the merger of adjacent plumes. For instance, Kaye and Linden [11] assumed that the mechanism driving merger is the passive advection between plumes placed side by side. Their model predicts a merging height that is in good agreement with experimental measurements. Later Linden and Kaye [12] adapted Kaye and Linden's model in the context of naturally ventilated buildings; they found that the merger of two coflowing plumes influences the stratification only if merger occurs below the ambient interface height expected for two noninteracting plumes. Extending the work of Kaye and Linden [11], Cenedese and Linden [13] proposed a piecewise equation describing the volume flux of two merging plumes through three different stages of plume evolution. In a separate effort, Rooney [14] developed a novel plume merger model by describing the boundaries of n merging plumes using velocity potential contours for n line sinks. Rooney [14] investigated the merging of an infinite row of plumes, then explored in a later study [15] the merging of n equally spaced plumes arranged around a circle. By the method of images, Rooney's latter study can be extended to the case of a plume in a corner of angle $2\pi/n$ where n , as argued by Rooney, remains integer valued; the noninteger case remains to be characterized. In a further extension of Rooney's later model [15] for plume merger, He and Lou [16] added linear stratification to the external ambient. Their theoretical predictions compare reasonably well with the output from analog numerical models, which are described in a companion study [17]. Even more recently, Li and Flynn [18,19] have extended Rooney's theory to include the effects of a nonidealized plume source, multiple rows, and crosswinds.

Studies of plume merger have helped guide our understanding of plume rise in the vicinity of vertical walls. For instance, Gao *et al.* [20,21] applied the aforementioned piecewise model of Cenedese and Linden [13] to study wall and corner plumes in a ventilated enclosure. Gao *et al.* [21] thereby determined the critical distance between the plume and the vertical boundary (wall or corner) below which ambient entrainment is restricted. Other wall plume studies have pursued different questions; e.g., Cooper and Hunt [22] and Kaye and Cooper [23] both considered plumes that emanate from a distributed source of buoyancy. Analogous to MTT, Cooper and Hunt [22] proposed a plume model using the entrainment assumption. Owing to the high-Reynolds number of the flow, they ignored the contribution of the wall shear stress. In Cooper and Hunt's ventilated filling-box experiments, they found that a complicated density stratification develops in the enclosure owing to horizontal intrusions that form due to the detrainment of plume fluid from the vertically distributed source. Kaye and Cooper [23] analyzed the effects of a finite source and of wall shear stress on vertically distributed plumes. They concluded that the reduced entrainment coefficient for wall-bounded plumes may be due to (1) the wall shear stress, (2) the restriction imposed by the wall on the engulfment of the largest eddies and on plume meandering, and (3) the nonideal source. More recently, Parker *et al.* [24] revealed that the entrainment rate per unit height for a two-dimensional wall plume is less than one-half the value of a line plume of equal source buoyancy flux situated far away from a wall. As argued by Parker *et al.* [24], the presence of the wall imposes no-slip and no-penetration boundary conditions, which carry similar importance in determining rates of entrainment. For three-dimensional wall plumes, Ezhova *et al.* [25] introduced a drag term into the classic MTT plume equations whereby the entrainment coefficient and drag coefficient are quantified from data derived from direct numerical simulations. Contrary to Parker *et al.* [24], Ezhova *et al.* [25] found that the volume flux of a three-dimensional wall plume is one-half of that expected for a conical plume whose rise is unimpeded by sidewalls.

The studies described above focus primarily on Boussinesq plumes where density differences are only important insofar as computing the buoyancy. However, there are many situations where density differences exceed $\sim 10\%$, plumes generated by fires being the oft-cited example. Compared to a fire source located at the room center, a fire source situated near a wall or corner is subject

to restricted entrainment and possibly leads to an increase in the temperature of smoke that accumulates below the ceiling. The study of Mowrer and Williamson [26] revealed that a fire in a corner may cause flashover with half the heat release rate expected for a fire located at the room center. Later Takahashi *et al.* [27] studied the effects of corners on flame heights and plume entrainment. Their experimental measurements showed that, in comparison to an isolated fire, a corner fire is characterized by reduced vertical velocities, a more moderate growth rate, and an extended flame height. A more recent study by McGrattan and Stroup [28] investigated the effect of an offset distance between a plume and a corner on the hot layer temperature and height. McGrattan and Stroup found that the corner effect is most important when the fire is just against the corner and that this effect fades quickly as the offset distance increases.

The above review indicates that the plume geometry plus the details of plume merger have a nontrivial effect on the manner in which turbulent entrainment is parameterized. In this spirit, the current study focuses on plume rise in a corner, a configuration that is commonly seen in practice but not as commonly studied, e.g., in the context of natural ventilation. Compared to the previous work of Rooney [15], the novelty of the present contribution is fourfold: (1) we generalize Rooney's model and thereby include noninteger values for n , (2) we propose an alternate entrainment assumption whereby the near-field entrainment is not reduced, (3) we extend Rooney's model to describe non-Boussinesq plume rise in a corner, and (4) we apply the present theory to the case of a naturally ventilated space.

Our paper is structured as follows: In Sec. II we first review Rooney's work in Secs. II A to II C, then in Secs. II D and II E we generalize Rooney's theory to model a plume in a corner of arbitrary angle. In Sec. III we propose an alternate entrainment formulation that relates the entrainment flux per unit height to the plume perimeter. In Sec. IV we formulate the analog non-Boussinesq theory. Thereafter, in Sec. V we adapt the models of Secs. II and IV to a naturally ventilated space driven by plume rise in a corner. In Sec. VI we draw conclusions.

II. BOUSSINESQ PLUME IN A CORNER

According to Turner [29] and Kaye and Linden [11], the induced flow into a turbulent plume can be treated as horizontal and irrotational and is akin to the flow resulting from a line sink. By extension, and considering the linearity of Laplace's equation, the entrainment flow into two or more plumes can be described by a superposition of line sinks. Moreover, and by the method of images, the configuration consisting of n plumes equally spaced around a circle is equivalent to the case of a plume situated in a corner with angle $2\pi/n$. In the following, we first prescribe the complex potential that describes the entrainment flow into a plume in a corner. Consistent with Rooney [15], we then describe the contours of equal velocity potential, which represent the mean plume boundaries at different heights.

A. Complex potential [15]

Following the idea of superposing line sinks, let the n line sinks in question be located at

$$Z_p = a e^{i2\pi p/n}, \quad p = 0, 1, \dots, n-1, \quad (1)$$

where $Z = x + iy = re^{i\theta}$, $a (>0)$ is a real constant [Fig. 1(a)] and n , for now, $\in \mathbb{N}$. The complex potential due to these n line sinks is given by

$$\Omega = -\frac{m}{2\pi} \ln(Z^n - a^n) = -\frac{m}{2\pi} \ln(Z^n - 1) - \frac{m}{2\pi} \ln a^n, \quad (2)$$

where $Z' = Z/a$ and m is the (uniform) strength of each individual line sink. Using polar coordinates, i.e., $Z' = \rho e^{i\theta}$ where $\rho = r/a$, and from $\Omega = \phi + i\psi$, the velocity potential, ϕ , and the stream function, ψ , are, respectively, given by

$$\phi = -\frac{m}{2\pi} \ln(\rho^{2n} - 2\rho^n \cos n\theta + 1)^{1/2}, \quad (3)$$

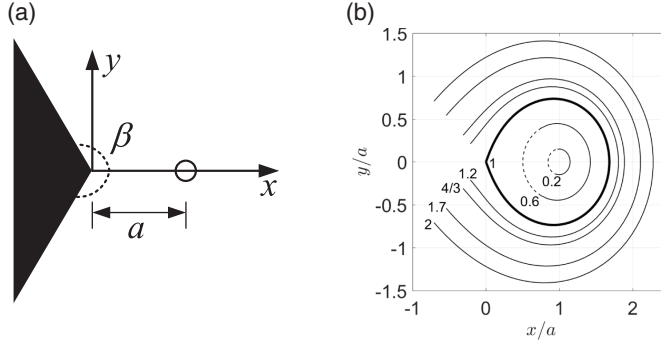


FIG. 1. (a) Top view of a plume in a corner of angle $\beta = 2\pi/n$. Here $n < 2$, but our analysis applies equally to the case $n \geq 2$. (b) Velocity potential contours for $n = 4/3$ ($\beta = 3\pi/2$). Contours are labeled according to their k value, k defined in (6). For $k < 1$, the solid and dashed curves denote the positive and negative square roots of (7), respectively. The thick solid curve corresponding to $k = 1$ represents the level of first contact.

$$\psi = -\frac{m}{2\pi} \tan^{-1} \left(\frac{\rho^n \sin n\theta}{\rho^n \cos n\theta - 1} \right). \quad (4)$$

Although (2)–(4) are derived assuming n to be integer-valued, we will show that for any real number $n \geq 1$, (2)–(4) apply for a line sink in a corner of angle $\beta = 2\pi/n$. As illustrated schematically in Fig. 1(a), the vertex of the corner is located at the origin and the plume source lies on the bisector of the angle β at a radial distance a from the origin. In polar coordinates, the two corner surfaces are described by $\theta = \pm\beta/2$. For solid surfaces, the no-penetration boundary condition should be satisfied, which implies that the velocity normal to the corner surface respects:

$$u_\theta|_{\theta=\pm\beta/2} = \frac{1}{r} \frac{\partial\phi}{\partial\theta} \Big|_{\theta=\pm\beta/2} = -\frac{m}{2\pi a} \frac{n\rho^{n-1} \sin n\theta}{\rho^{2n} - 2\rho^n \cos n\theta + 1} \Big|_{\theta=\pm\beta/2} = 0. \quad (5)$$

Thus, the corner surfaces are also streamlines of the flow. Moreover, the flow always includes a stagnation point located exactly at the origin. In this sense, (2) with $n \geq 1$ is a stagnation flow that is similar to another common type of stagnation flow in a corner of angle π/n , i.e., the stagnation flow described by $\Omega = aZ^n$.

Contours of equal velocity potential are described by

$$\rho^{2n} - 2\rho^n \cos n\theta + 1 = k^2, \quad (6)$$

where $k > 0$ is a constant. Solving for ρ and θ separately yields

$$\rho = [\cos n\theta \pm (k^2 - \sin^2 n\theta)^{1/2}]^{1/n}, \quad (7)$$

$$\theta = \pm \frac{1}{n} \cos^{-1} \left(\frac{\rho^{2n} + 1 - k^2}{2\rho^n} \right). \quad (8)$$

For $n = 4/3$ ($\beta = 3\pi/2$), a set of velocity potential contours is illustrated in Fig. 1(b). The maximum radial extent occurs at $\theta = 0$ and is given by

$$\rho_{\max} = (k + 1)^{1/n}. \quad (9)$$

The minimum radial extent is given by a piecewise function that reads

$$\rho_{\min} = \begin{cases} (1 - k)^{1/n}, & k \leq 1 \\ (k - 1)^{1/n}, & k > 1. \end{cases} \quad (10)$$

From (9) and (10), the cross-sectional area enclosed by a velocity potential contour is given by

$$\hat{A} \equiv \frac{A}{a^2} = \begin{cases} 2 \int_{\rho_{\min}}^{\rho_{\max}} \theta_+ \rho \, d\rho, & k \leq 1 \\ \frac{1}{2} \int_{-\pi/n}^{\pi/n} \rho_+^2 \, d\theta, & k > 1, \end{cases} \quad (11)$$

where the subscript + corresponds to the positive root in (7) and (8).

The entrainment flow speed can be obtained from $q = \left| \frac{d\Omega}{dz} \right|$, which is given by

$$q = \frac{m}{2\pi a} \frac{n\rho^{n-1}}{k}. \quad (12)$$

Thus the flow speed at the maximum radial extent, ρ_{\max} (9), is expressed as

$$q_e = \frac{m}{2\pi a} \frac{n(k+1)^{(n-1)/n}}{k}. \quad (13)$$

Note that q_e is the maximum entrainment speed measured along a velocity potential contour.

B. Entrainment flux

On any of the velocity potential contours shown in Fig. 1(b), the (irrotational) entrainment flow velocity is everywhere orthogonal to the contour. The associated entrainment flux can be evaluated using the stream function (4). For $k \leq 1$, the entrainment flux per unit height, E , can be computed from

$$E = 2(\psi(\rho_{\max}, 0) - \psi(\rho_{\min}, 0)) = -\frac{m}{\pi}(0 - \pi) = m. \quad (14)$$

An identical result is obtained when $k > 1$:

$$E = 2(\psi(\rho_{\max}, 0) - \psi(\rho_{\min}, \pi/n)) = -\frac{m}{\pi}(0 - \pi) = m. \quad (15)$$

Using (13), the entrainment flux can be related to q_e by

$$E = m = a \frac{2\pi k}{n(k+1)^{(n-1)/n}} q_e. \quad (16)$$

C. Boussinesq plume equations

Through a rearrangement of the MTT plume equations, Rooney [14] proposed a pair of generalized equations for a Boussinesq plume in an unstratified ambient. This pair reads as follows:

$$A \frac{d}{dz} \left(\frac{1}{2} w^2 \right) = Ag' - wE, \quad (17)$$

$$\frac{d}{dz} (Aw) = E, \quad (18)$$

where w and g' are the plume mean vertical velocity and reduced gravity, respectively. The set of Eqs. (17) and (18) is closed by an entrainment assumption, i.e., $q_e = \alpha w$, where α is an empirical entrainment coefficient. Equations (17) and (18) can be written in nondimensional form as

$$\frac{d\hat{w}}{d\hat{z}} = \frac{1}{\hat{Q}\hat{w}} - \frac{f_e \hat{w}^2}{\hat{Q}}, \quad (19)$$

$$\frac{d\hat{Q}}{d\hat{z}} = f_e \hat{w}, \quad (20)$$

where

$$f_e = \frac{2\pi k}{n(k+1)^{(n-1)/n}}. \quad (21)$$

Meanwhile, \hat{w} , \hat{Q} , and \hat{z} respectively indicate the nondimensional vertical velocity, plume volume flux, and vertical coordinate. These parameters are related to their dimensional analogues via

$$w = \alpha^{-1/3} F^{1/3} a^{-1/3} \hat{w}, \quad Q = \alpha^{-1/3} F^{1/3} a^{5/3} \hat{Q}, \quad z = \alpha^{-1} a \hat{z}. \quad (22)$$

Here $F = Awg'$ is the plume buoyancy flux. In similar fashion, we define the plume momentum flux as $M = Qw$. The plume momentum flux is important because it appears in the flux-balance parameter, Γ , which is defined as [30]

$$\Gamma(z) \equiv \frac{5}{8\pi^{1/2}\alpha} \frac{FQ^2}{M^{5/2}} = \frac{5}{8\pi^{1/2}\hat{A}^{1/2}\hat{w}^3}. \quad (23)$$

The flux-balance parameter is useful because it is a single nondimensional number that quantifies the departure of the plume from a pure-plume balance with $\Gamma = 1$.

To solve (19) and (20), we first assign a small value for k , e.g., $k_0 = 0.001$ whereupon the source cross-sectional area, \hat{A}_0 , can be obtained using (11). Then, for prescribed $\Gamma_0 \equiv \Gamma(z=0)$, the source vertical velocity, \hat{w}_0 , can be determined using (23). In turn, \hat{Q}_0 is obtained from $\hat{Q} = \hat{A}_0 \hat{w}_0$. Equations (19) and (20) are then integrated using a fourth-order Runge-Kutta method. Assuming a pure-plume balance at the source, $\Gamma_0 = 1$, a near-field virtual origin, \hat{z}_{vn} , may be applied, where

$$\hat{z}_{vn} = \frac{5}{6} \left(\frac{0.001}{n} \right). \quad (24)$$

D. Plume boundary curvature

The curvature at any point on a velocity potential contour is given by

$$\kappa(\theta) = \frac{|2\left(\frac{d\rho}{d\theta}\right)^2 + \rho^2 - \rho\frac{d^2\rho}{d\theta^2}|}{\left[\rho^2 + \left(\frac{d\rho}{d\theta}\right)^2\right]^{3/2}}. \quad (25)$$

Thus the characteristic curvature at $\theta = \pm\pi/n$ is given by

$$\kappa_1 = \frac{|k-n|}{k(k-1)^{1/n}}, \quad (26)$$

where $k > 1$. Thus $\kappa_1 = 0$ requires $k = n$, which is consistent with $k = 2$ for the merging of $n = 2$ plumes as studied by Li and Flynn [18]. In physical terms, $k = n$ represents the vertical elevation where the plume boundary is no longer concave and thereafter the plume, which had until this elevation appeared significantly distorted, exhibits a more uniform radius of curvature. When $k = 1$ [thick solid curve of Fig. 1(b)], $\kappa_1 \rightarrow \infty$ implying that the plume distortion is maximum. In the following, we shall define $k = 1$ and $k = n$ as two contact heights, denoted as $\hat{z}_{c,1}$ and $\hat{z}_{c,2}$, respectively. In particular, and by the method of images, $\hat{z}_{c,2}$ is analogous to the height of full merger defined in Kaye and Linden [11].

E. Representative solutions

The major difference with Rooney's work up to this point is that we consider n to be noninteger. For noninteger n , Rooney [15] argued that the potential field described by (2) is discontinuous on the negative real axis. This discontinuity, as we have discussed in Sec. II A, is not an issue when considering a plume in a corner of arbitrary angle. To wit, the corner surfaces are always streamlines of the flow; see (5). On this basis, and by setting n to be noninteger, we aim to examine (1) whether the theoretical results still approach the correct near- and far-field similarity solutions (see Sec. 3.2

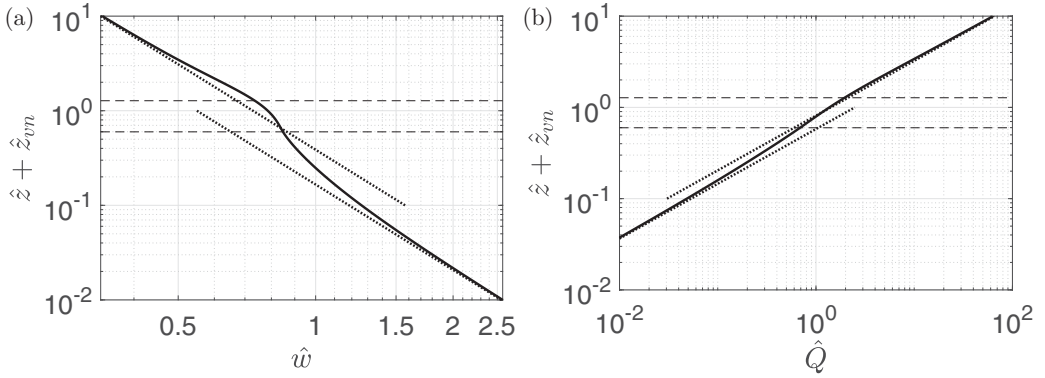


FIG. 2. Log-log plot showing the vertical variation of \hat{w} (a) and \hat{Q} (b) for $n = 7/3$ ($\beta = 6\pi/7$). The dotted lines denote the respective near- and far-field similarity solutions, as given in Sec. IV B but with $\eta = 1$ where η is the ratio of plume density to ambient density. The lower and upper dashed horizontal lines denote $\hat{z}_{c,1} = 0.60$ and $\hat{z}_{c,2} = 1.28$, respectively. $\hat{z}_{c,1}$ ($\hat{z}_{c,2}$) is determined as the height where k is closest to 1 (n).

of 15; see also Sec. IV B with $\eta = 1$) and (2) whether the theoretical results vary smoothly from integer to noninteger n values.

Representative results showing the plume nondimensional vertical velocity and volume flux for the $n = 7/3$ ($\beta = 6\pi/7$) case are illustrated in Fig. 2. Both panels confirm that this noninteger case approaches the near- and far-field similarity solutions. Figure 2(a) shows that the vertical velocity first overshoots the far-field similarity limit then relaxes back, a trend also observed in Fig. 3(a) of Rooney [15]. A linear extrapolation of the $(\hat{Q}/\hat{w})^{1/2}$ data for $9 < \hat{z} \leq 10$ (not shown) yields a far-field virtual origin $\hat{z}_{vf} = -0.20$ ¹. For a range of n values, we plot $\hat{z}_{c,1}$, $\hat{z}_{c,2}$ and \hat{z}_{vf} in Fig. 3.

¹The negative value seen here indicates a virtual origin that is situated above (i.e., downstream of) the physical source. When, as in (24), the virtual source is positive, the virtual origin is instead situated below the physical source.

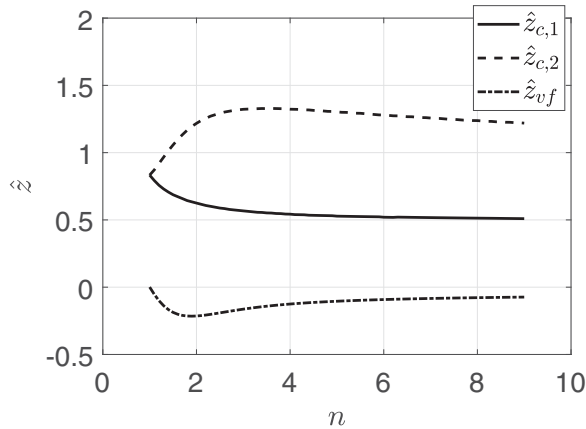


FIG. 3. $\hat{z}_{c,1}$, $\hat{z}_{c,2}$, and \hat{z}_{vf} vs n ($\beta = 2\pi/n$). $\hat{z}_{c,1}$ and $\hat{z}_{c,2}$ are two contact heights corresponding to $k = 1$ and $k = n$, respectively. \hat{z}_{vf} is the far-field virtual origin. In all cases, $\Gamma_0 = 1$. Virtual origin corrections are included in the manner of (24).

The profiles in Fig. 3 show that $\hat{z}_{c,1}$ and \hat{z}_{vf} reach their respective asymptotic values for $n \gtrsim 4$. The nonmonotonic variation of $\hat{z}_{c,2}$ with n is due to the competing effects of plume distortion and corner angle. When n is small, the plume distortion effect is expected to be small thus leading to small $\hat{z}_{c,2}$. By contrast, larger n implies smaller corner angle so that plume easily fills the corner, which results in a decrease in $\hat{z}_{c,2}$.

III. ALTERNATE ENTRAINMENT CLOSURE

Recall that the entrainment assumption described in Sec. IIC, $q_e = \alpha w$, relates the maximum entrainment velocity (13) to the mean vertical velocity of the plume. Note also that the entrainment flux E is related to q_e by $E = af_e q_e$ (16), which, for a prescribed E , requires the minimum f_e because q_e is maximum. The parameter f_e is interpreted as the nondimensional effective entrainment perimeter in Li and Flynn [19]. Using the aforementioned (MTT) entrainment assumption, Rooney [15] revealed that the predicted Γ shows an unusual, nonmonotonic variation with height. To achieve a more regular Γ profile, Rooney [15] proposed an empirical function for the entrainment correction that includes k , Γ , and a model constant S ; see his Eq. (3.16). Li and Flynn [18] incorporated an empirical correction factor that depends only on the plume boundary curvature, κ of (25). Overall, the deficiencies of these previous entrainment correction formulations are twofold: (1) a lack of theoretical basis and (2) an overprediction of the reduction in entrainment in the near field. As regards (2), plume entrainment can be assumed to be unaffected below the height of first contact, which is supported by the experimental studies of Kaye and Linden [11] and Cenedese and Linden [13]. To resolve this deficiency without introducing more empirical factors, we consider a smaller entrainment velocity, e.g., $q_l = E/l$, which denotes the mean entrainment velocity per unit contour length l . Assuming $q_l = \alpha w$, the entrainment flux per unit height, E , is given by

$$E = \alpha w l = \alpha w a f_l, \quad (27)$$

where the parameter f_l is defined as $f_l = \hat{l} \equiv l/a$. Analogous to the plume cross section \hat{A} , \hat{l} can be obtained by integration over ρ or θ using (A5) of Rooney [15]. In the case of undistorted plume cross section (and unaffected entrainment) below the first contact height, the nondimensional entrainment perimeter can be expressed as $2(\pi\hat{A})^{1/2}$.

A comparison of f_e , f_l , and $2(\pi\hat{A})^{1/2}$ is shown in Fig. 4. As expected, $f_e \geq f_l$ and the deviation is largest at $k = 1$. Moreover, f_e increases monotonically with k , whereas f_l first increases then decreases sharply at $k = 1$ and thereafter increases again. The insets to Figs. 4(a) and 4(b) show that f_l and $2(\pi\hat{A})^{1/2}$ closely align with each other and the differences become distinguishable only when k is close to unity. This close match implies that the present model aligns with the measurements of Kaye and Linden [11] and Cenedese and Linden [13], who, to reiterate, found that entrainment was little impacted below $\hat{z}_{c,1}$.

For $n = 2$, the effective entrainment is defined by $Q_{\text{eff}} = (Q/Q_{(n=1)})^{3/4}$ where $Q_{(n=1)}$ denotes the volume flux of an isolated plume [13]. Figure 5(a) shows the variation of Q_{eff} with \hat{z} for the original (constant entrainment coefficient) MTT model, Rooney [15], the entrainment model represented by (27) and the piecewise model of Cenedese and Linden [13]. In the latter case (and again assuming $n = 2$), the equation for the effective entrainment reads as follows:

$$Q_{\text{eff, CL}} = \begin{cases} 1, & \hat{z} < 0.70, \\ (\hat{z}/2)^{-5/4} (0.73\hat{z}/2 - 0.082)^{3/4}, & 0.70 \leq \hat{z} \leq 0.88, \\ \frac{1}{2^{1/2}} \left(1 + \frac{0.12}{\hat{z}/2}\right)^{5/4}, & \hat{z} \geq 0.88, \end{cases} \quad (28)$$

where the subscript CL stands for Cenedese and Linden [13]. Note that (28), which has been validated by the filling box experiments of Cenedese and Linden [13], applies only for $n = 2$. Figure 5(a) shows that the present model (solid black curve) yields better agreement with Cenedese

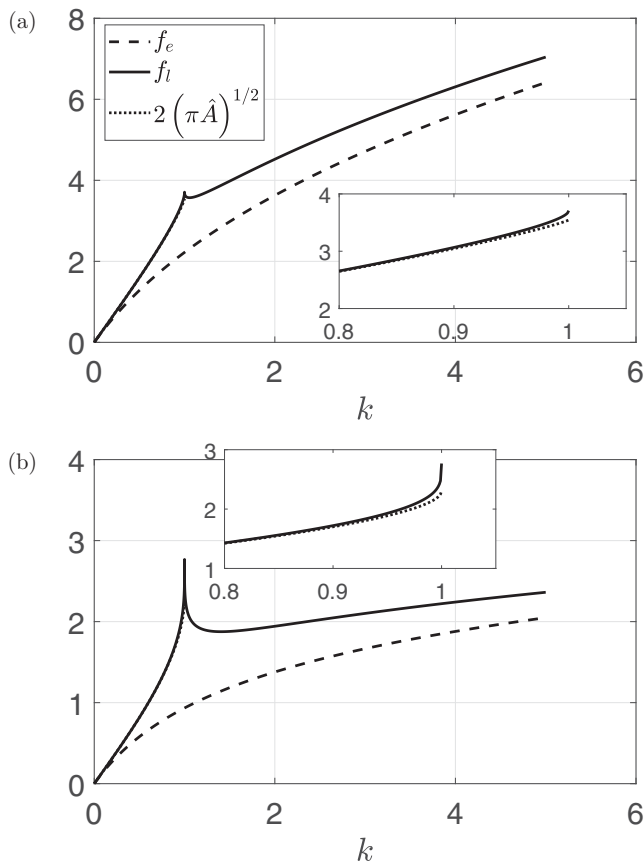


FIG. 4. Comparison of f_e , f_l , and $2(\pi\hat{A})^{1/2}$ as functions of k for $n = 2$ (a) and $n = 4$ (b). f_e is defined by (21), and $f_l = l/a$ where l denotes the contour length.

and Linden's model compared to the other models, especially in the near-field where the effective entrainment is constant. Complementing the data from Fig. 5(a), the two contact heights predicted by the same four models are summarized in Table I. Significantly, (27) predicts the smallest $\hat{z}_{c,1}$, which is due to its enhanced entrainment below $\hat{z}_{c,1}$ compared to the MTT and Rooney [15] models. Cenedese and Linden [13] predicts the largest $\hat{z}_{c,1}$ because they assume that the plume interaction before the point of first contact is mutual advection rather than plume distortion. Note, moreover, that $\hat{z}_{c,2}$ predicted by (27) is closest to that of Cenedese and Linden [13]. For $n = 4$, Fig. 5(b) shows similar profiles to those displayed in Fig. 5(a). Note that the near-field kink observed at $\hat{z} \simeq 0.3$ in the solid curve of Fig. 5(b) corresponds to the kink in the solid curve of Fig. 4(b).

TABLE I. Contact heights predicted by MTT, Rooney [15], the present model (27) and Cenedese and Linden [13] for the $n = 2$ case. $\hat{z}_{c,1}$ ($\hat{z}_{c,2}$) is defined as the height where $k = 1$ ($k = n$); see Sec. IID.

	MTT	Rooney [15]	Present model	Cenedese and Linden [13]
$\hat{z}_{c,1}$	0.63	0.55	0.47	0.70
$\hat{z}_{c,2}$	1.22	1.01	0.91	0.88

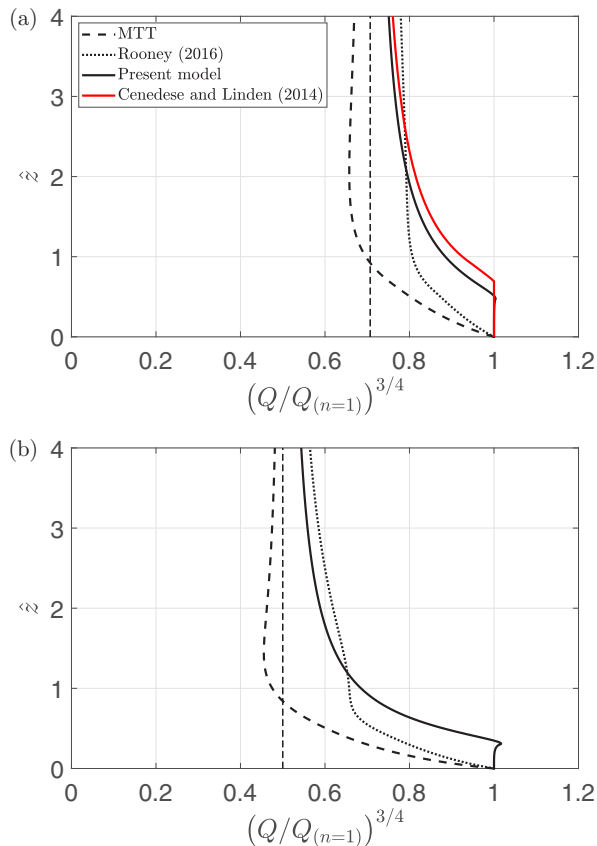


FIG. 5. Effective entrainment vs height for four different theoretical models. (a) $n = 2$. The vertical dashed line represents the far-field limit of $2^{-1/2}$. (b) $n = 4$. The vertical dashed line represents the far-field limit of $4^{-1/2} = 1/2$. The Cenedese and Linden [13] solution is here omitted because their model is restricted to $n = 2$.

IV. NON-BOUSSINESQ PLUME IN A CORNER

A. Non-Boussinesq plume equations

Following the pioneering work of Rooney and Linden [31], the top-hat governing equations for a non-Boussinesq plume rising through an unstratified ambient read

$$\frac{d}{dz}(\rho Aw) = \rho_a E \quad (\text{Mass}), \quad (29)$$

$$\frac{d}{dz}(\rho Aw^2) = -gA(\rho - \rho_a) \quad (\text{Momentum}), \quad (30)$$

$$\frac{d}{dz}(Aw) = E \quad (\text{Volume}), \quad (31)$$

where ρ is the plume density, ρ_a is the ambient fluid density, A is the plume cross-sectional area, w is the mean vertical velocity, E is the rate of entrainment per unit height, and g is gravitational acceleration. Letting $\eta = \rho/\rho_a$, the mass (29) and volume (31) evolution equations indicate that the density deficit flux, $F = gAw(1 - \eta)$, is constant. Equation (30) can be rewritten, with the aid of

(29), as

$$A \frac{d}{dz} \left(\frac{1}{2} w^2 \right) = Ag \frac{1-\eta}{\eta} - \frac{wE}{\eta}. \quad (32)$$

In the Boussinesq limit $\eta \rightarrow 1$, and (32) reduces to (3.1a) of Rooney [15].

For non-Boussinesq plumes, Rooney and Linden [31] used their similarity solutions to derive the entrainment assumption, which reads

$$u_e = \alpha \eta^{1/2} w. \quad (33)$$

Assuming $u_e = E/l$ [cf. Eq. (27)], E is given by

$$E = \alpha \eta^{1/2} w l. \quad (34)$$

Defining the volume flux as $Q = Aw$ and using (34), (32), and (31) can be respectively rewritten as

$$\frac{dw}{dz} = \frac{F}{\eta Q w} - \frac{\alpha l}{\eta^{1/2}} \frac{w^2}{Q}, \quad (35)$$

$$\frac{dQ}{dz} = \alpha l \eta^{1/2} w. \quad (36)$$

Moreover, the conservation of density deficit flux, $dF = 0$, yields

$$\frac{d\eta}{1-\eta} = \frac{dQ}{Q}. \quad (37)$$

Using the density deficit flux, F , and the characteristic length scale a , the vertical velocity, volume flux and vertical distance can be nondimensionalized as in (22). On this basis, (35) to (37) can be rewritten as

$$\frac{d\hat{w}}{d\hat{z}} = \frac{1}{\eta \hat{Q} \hat{w}} - \frac{\hat{w}^2}{\eta^{1/2} \hat{Q}} \hat{l}, \quad (38)$$

$$\frac{d\hat{Q}}{d\hat{z}} = \eta^{1/2} \hat{w} \hat{l}, \quad (39)$$

$$\frac{d\eta}{d\hat{z}} = (1-\eta) \eta^{1/2} \frac{\hat{w}}{\hat{Q}} \hat{l}. \quad (40)$$

The flux-balance parameter for non-Boussinesq plumes, Γ_{nb} , is defined as [32]

$$\Gamma_{nb}(z) = \frac{5FG^2}{8\alpha\pi^{1/2}M^{5/2}} = \frac{5}{8\pi^{1/2}\eta^{1/2}} \hat{A}^{-1/2} \hat{w}^{-3}, \quad (41)$$

where the mass flux is $G = \eta Aw$, the momentum flux is $M = \eta Aw^2$ and the nondimensional cross-sectional area is $\hat{A} = \hat{Q}/\hat{w} = A/a^2$. To solve (38)–(40), we first assign a small value of k , e.g., $k_0 = 0.01$ at the source $z = 0$, thus the source cross-sectional area $\hat{A}_0 \equiv \hat{A}(z = 0)$ can be determined using (11). By setting $\Gamma_{nb,0} \equiv \Gamma_{nb}(z = 0)$ and $\eta_0 \equiv \eta(z = 0)$ separately, we can then determine $\hat{w}_0 \equiv \hat{w}(z = 0)$ from (41). With all the source parameters set, (38)–(40) can be integrated in height using a fourth-order Runge-Kutta method. Considering the finite source at $z = 0$, a near-source virtual origin correction is applied using the methodology of Carlotti and Hunt [32]. For the special case of $\Gamma_{nb,0} = 1$, the near-field virtual origin is located at

$$z_{vn} = (Q_0 \eta_0)^{3/5} F^{-1/5} \kappa^{-3/5}, \quad (42)$$

where $Q_0 \equiv Q(z = 0)$ and $\kappa = \frac{3^{5/3}(2\pi)^{2/3}}{5^{4/3}}\alpha^{4/3}$. In terms of nondimensional variables, (42) can be written as

$$\hat{z}_{vn} = \frac{5^{4/5}}{3(2\pi)^{2/5}}\hat{Q}^{3/5}\eta_0^{3/5}. \quad (43)$$

B. Near- and far-field similarity solutions

In the near field, the plume tends to be axisymmetric and similarity solutions are possible. According to Rooney and Linden [31], analytical solutions to (35)–(37) are given by

$$w = \left(\frac{3}{4}\right)^{1/3} \left(\frac{6\alpha}{5}\right)^{-2/3} \pi^{-1/3} F^{1/3} z^{-1/3}, \quad (44)$$

$$Q = \frac{6\alpha}{5} \left(\frac{9\alpha}{10}\right)^{1/3} \pi^{2/3} \eta^{-1} F^{1/3} z^{5/3}, \quad (45)$$

$$\Delta = \left(\frac{4}{3}\right)^{1/3} \left(\frac{6\alpha}{5}\right)^{-4/3} \pi^{-2/3} F^{2/3} g^{-1} z^{-5/3}, \quad (46)$$

where $\Delta = \frac{1-\eta}{\eta}$. The counterpart nondimensional solutions for w and Q are given, respectively, as

$$\hat{w} = \frac{5}{6} \left(\frac{9}{10}\right)^{1/3} \pi^{-1/3} \hat{z}^{-1/3}, \quad \hat{Q} = \frac{6}{5} \left(\frac{9}{10}\right)^{1/3} \pi^{2/3} \eta^{-1} \hat{z}^{5/3}. \quad (47)$$

The far-field flow for a plume in a corner of angle $2\pi/n$ is equivalent to n merged plumes with buoyancy flux nF . Therefore, and replacing F with nF in (44), we obtain the far-field similarity solution for w . By contrast, the far-field similarity solution for Q is given by [15]

$$Q = \frac{1}{n} \frac{6\alpha}{5} \left(\frac{9\alpha}{10}\right)^{1/3} \pi^{2/3} \eta^{-1} (nF)^{1/3} z^{5/3} \quad \Rightarrow \quad \hat{Q} = \frac{6}{5} \left(\frac{9}{10}\right)^{1/3} \eta^{-1} \left(\frac{\pi}{n}\right)^{-2/3} \hat{z}^{5/3}. \quad (48)$$

It is expected that the plume is Boussinesq in the far-field thus (48) is identical to the counterpart Boussinesq far-field similarity solution. By extension, the modified flux-balance parameter $\Gamma_{nb, m} \equiv n^{1/2} \Gamma_{nb}$ tends to unity in the far field.

C. Representative solutions

For $n = 2$, $\eta_0 = 0.4$ and $\Gamma_{nb, 0} = 1$, solutions to (38)–(40) are illustrated in Fig. 6. Analogous to Figs. 2(a) and 2(b), Figs. 6(a) and 6(b) show that the plume vertical velocity and volume flux approach their respective near- and far-field similarity limits. The density profile shown in Fig. 6(c) indicates that non-Boussinesq effects are important only near the source. Assuming that the demarcation between the Boussinesq and non-Boussinesq regions is defined as the height, z_{nb} , where $\eta = 0.9$, the non-Boussinesq region for the case considered in Fig. 6 spans $0 < \hat{z} \leq \hat{z}_{nb} = 0.012$. Also evident from Fig. 6(c) is that the non-Boussinesq height \hat{z}_{nb} is considerably smaller than the first contact height, $\hat{z}_{c, 1}$; see the lower dashed line in Fig. 6(c). Figure 6(d) reveals that $\Gamma_{nb, m}$ is almost constant below $\hat{z}_{c, 1}$; this is consistent with the fact that the vertical velocity and volume flux closely align with the respective self-similar solutions below $\hat{z}_{c, 1}$; see Figs. 6(a) and 6(b).

For fixed $\Gamma_{nb, 0} = 1$ and $\eta_0 = 0.4$, $\hat{z}_{c, 1}$, $\hat{z}_{c, 2}$ and \hat{z}_{nb} are plotted as functions of n in Fig. 7. For a range of η_0 from 0.05 to 0.95, we have found that the curves of $\hat{z}_{c, 1}$ and $\hat{z}_{c, 2}$ versus n are almost identical (not shown), which indicates that non-Boussinesq effects do not dictate the heights of contact between the plume and the corner. This is also implied by Fig. 7 in that \hat{z}_{nb} is small compared to $\hat{z}_{c, 1}$ and $\hat{z}_{c, 2}$. As we indicate in Sec. IV D 1, the conclusion $\hat{z}_{nb} \ll \hat{z}_{c, 1}, \hat{z}_{c, 2}$ holds in general for small source plumes.

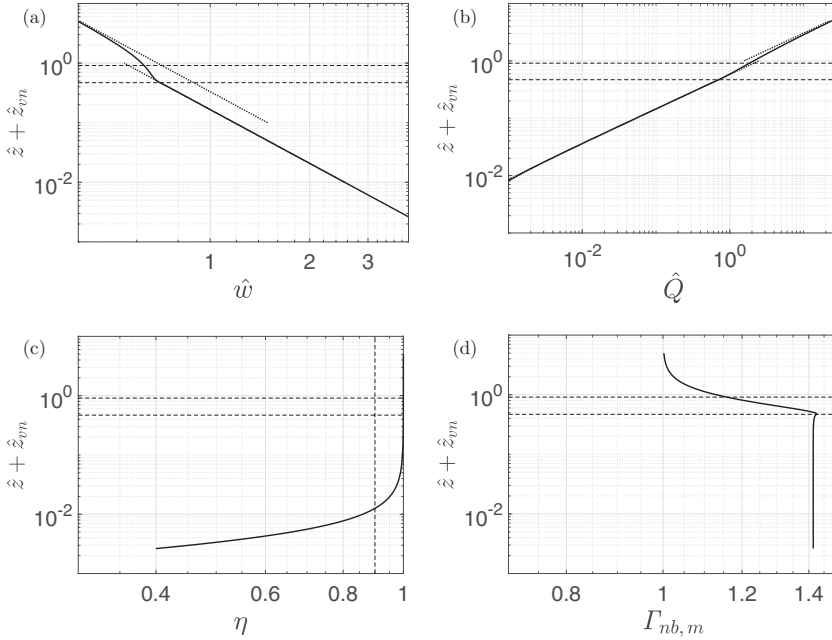


FIG. 6. Representative results of the nondimensional vertical velocity (a), volume flux (b), density (c), and modified flux-balance parameter (d) for $n = 2$, $\eta_0 = 0.4$ and $\Gamma_{nb,0} = 1$. The dotted lines in (a) and (b) denote the near- and far-field similarity limits, respectively. The vertical dashed line in (c) denotes $\eta = 0.9$. In all panels, the lower and upper horizontal dashed lines denote the contact heights defined in Sec. II D.

D. Non-Boussinesq height

1. Small source plumes

Further to Figs. 6 and 7, it is necessary to examine the non-Boussinesq height, \hat{z}_{nb} , for arbitrary plume source conditions and corner angles. For a point-source pure plume in an unbounded, uniform ambient, Woods [33] derived the vertical length scale over which non-Boussinesq effects

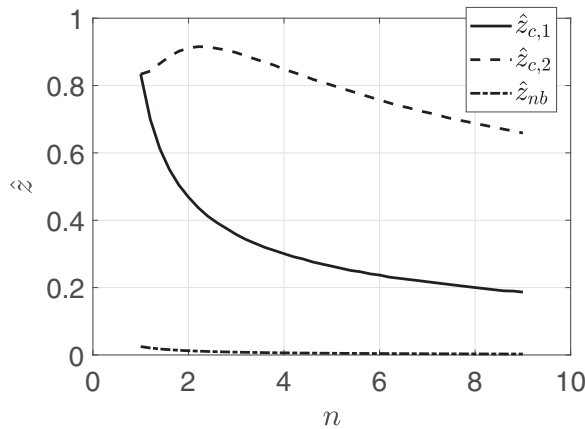


FIG. 7. $\hat{z}_{c,1}$, $\hat{z}_{c,2}$, and \hat{z}_{nb} vs n ($\beta = 2\pi/n$). $\hat{z}_{c,1}$ and $\hat{z}_{c,2}$ are two contact heights corresponding to $k = 1$ and $k = n$, respectively. \hat{z}_{nb} is defined as the point at which $\eta = 0.9$. In all cases, $\Gamma_0 = 1$ and $\eta_0 = 0.4$. Virtual origin corrections are included in the manner of (43).

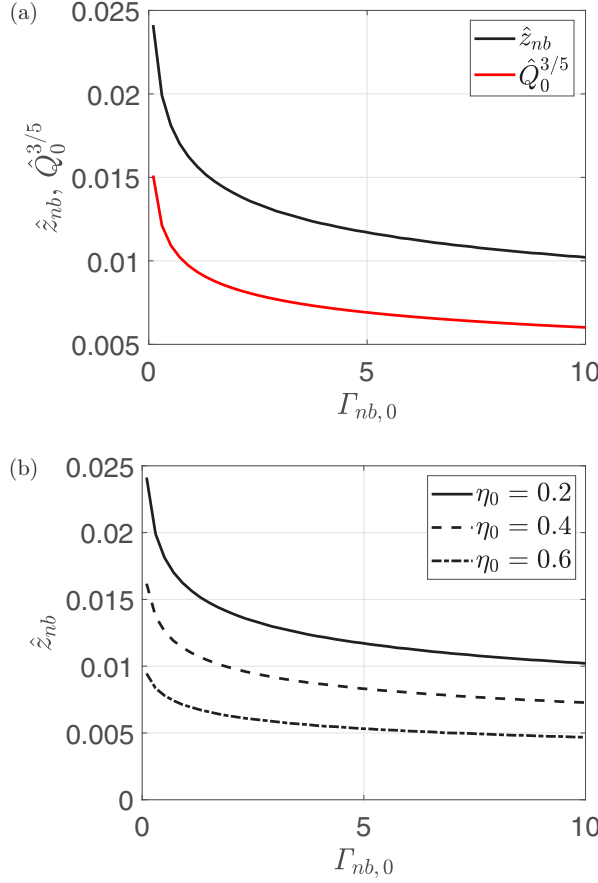


FIG. 8. (a) \hat{z}_{nb} and $\hat{Q}_0^{3/5}$ vs $\Gamma_{nb,0}$ for $n=2$ and $\eta_0=0.2$. (b) \hat{z}_{nb} vs $\Gamma_{nb,0}$ for $n=2$ and different η_0 . \hat{z}_{nb} is defined as the point at which $\eta=0.9$. $\hat{Q}_0^{3/5}$ (50) is a theoretically derived scaling height over which non-Boussinesq effects are important.

are important:

$$z_{nb \rightarrow b} = \left(\frac{F^2}{g^3 \alpha^4} \right)^{1/5}. \quad (49)$$

The above equation can be nondimensionalized in the manner of (22) whereby

$$\hat{z}_{nb \rightarrow b} = \hat{Q}_0^{3/5}. \quad (50)$$

For small and fixed $\hat{A}_0 = 10^{-4}$, $n=2$ and $\eta_0=0.2$, we plot \hat{z}_{nb} and $\hat{Q}_0^{3/5}$ versus $\Gamma_{nb,0}$ in Fig. 8. A virtual origin correction is not considered here because \hat{z}_{vn} is small compared to \hat{z}_{nb} . The curves in Fig. 8(a) show that \hat{z}_{nb} and $\hat{Q}_0^{3/5}$ are of the same order, which is consistent with the findings of Woods [33]. For $\hat{A}_0 = 10^{-4}$ and $n=2$, Fig. 8(b) shows \hat{z}_{nb} versus $\Gamma_{nb,0}$ for different η_0 . It is observed that \hat{z}_{nb} decreases with η_0 , which is consistent with the fact that $\hat{Q}_0^{3/5}$ also decreases with increasing η_0 . For the same source conditions but with different n , i.e., different corner angles, we find that the curves align closely with those in Fig. 8. This is consistent with Fig. 7, which indicates that \hat{z}_{nb} varies by only a small amount, particularly for $n \gtrsim 2$.

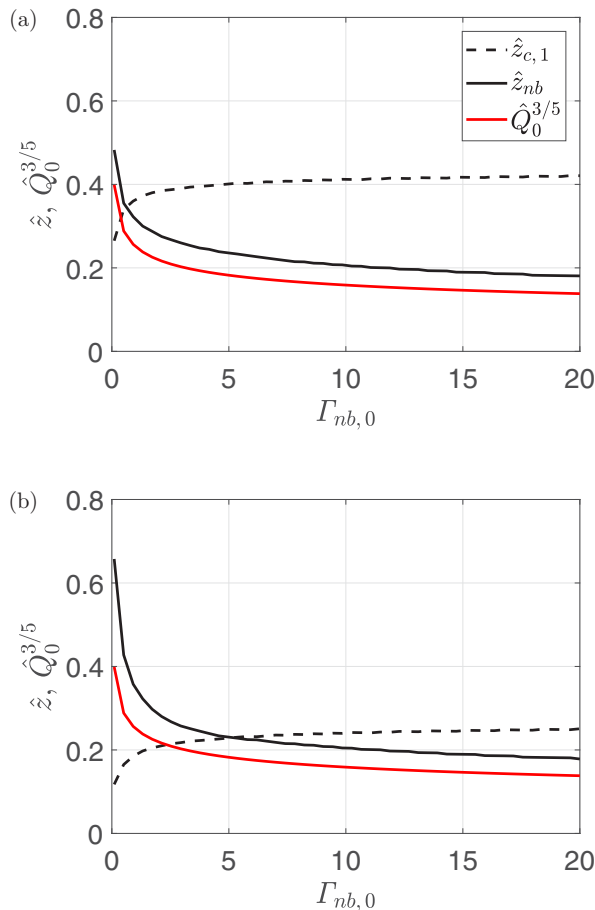


FIG. 9. \hat{z}_{nb} , $\hat{Q}_0^{3/5}$ and $\hat{z}_{c,1}$ vs $\Gamma_{nb,0}$ for $n = 2$ (a) and $n = 4$ (b). In both panels, $\eta_0 = 0.4$. \hat{z}_{nb} is defined as the point at which $\eta = 0.9$. $\hat{Q}_0^{3/5}$ (50) is a theoretically derived scaling height over which non-Boussinesq effects are important.

2. Large source plumes

When the plume source diameter is nontrivial compared to the distance between the plume center and corner vertex, the non-Boussinesq height is expected to be non-negligible compared to the first contact height. Strictly speaking, the theory in Sec. IV is applicable to plume sources close to ideal. For large source plumes, a large source area \hat{A}_0 is mapped to a relatively large k_0 , which corresponds to an already distorted plume source. Nonetheless, we still regard the aforementioned theory as a reasonable approximation for large source plumes in a corner, provided $k_0 < 1$. This approximation can be justified by the fact that the effect of distortion on entrainment becomes significant only when k is close to unity; see Fig. 4. To obtain some representative results, we first choose a source area $\hat{A}_0 = 0.08$, which can be mapped to $k_0 = 0.32$ when $n = 2$ and to $k_0 = 0.60$ when $n = 4$. Then by solving (38)–(40), we plot \hat{z}_{nb} , $\hat{Q}_0^{3/5}$ and $\hat{z}_{c,1}$ versus $\Gamma_{nb,0}$ in Fig. 9. In contrast to Fig. 7, Fig. 9 shows that \hat{z}_{nb} is comparable to $\hat{z}_{c,1}$; in fact, $\hat{z}_{nb} > \hat{z}_{c,1}$ when $\Gamma_{nb,0}$ is small (thus $\hat{Q}_0^{3/5}$ is large). Comparing the relative magnitude of \hat{z}_{nb} versus $\hat{z}_{c,1}$ in Figs. 9(a) and 9(b), non-Boussinesq effects are more pronounced in case of smaller corner angles. This finding is qualitatively consistent with the experimental observation that a right-angled corner has significant effects on the flame height and plume temperature while a wall does not [28]. Later in Sec. VB we validate the present

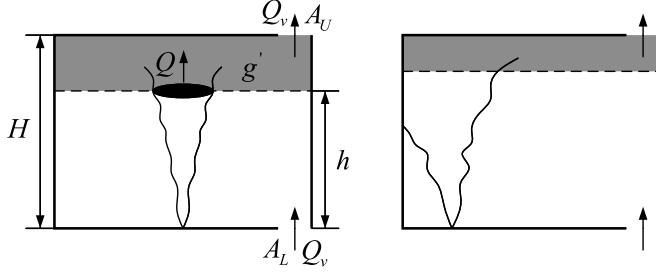


FIG. 10. Schematics of centered (left) and wall-bounded (right) plumes in naturally ventilated enclosures. The interface height is h , and the total room height is H .

non-Boussinesq plume theory with previously collected experimental measurements of area source fire plumes.

V. APPLICATIONS TO FLOWS IN BUILDINGS

A. Boussinesq plume

Following the seminal work of Linden *et al.* [3], we consider the application of the above results in Sec. II to a single-zone, naturally ventilated enclosure having a lower level vent of area A_L and an upper level vent of area A_U . The vents connect the enclosure (or room) to a much larger quiescent external environment; see Fig. 10. As a result of the thermal forcing imparted by the plume, a two-layer stratification develops over time. Fluid exchange between the upper and lower layers of Fig. 10 is through ambient entrainment into the ascending plume, which has the effect of transporting lower layer fluid across the ambient interface and into the upper layer. The ventilation volume flux, i.e., the flow rate through the lower and upper vents, can be computed by considering the hydrostatic pressure difference between the room and the ambient. To wit,

$$Q_v = A^* [g'_u (H - h)]^{1/2}, \quad (51)$$

where g'_u is the reduced gravity of the upper layer and the effective vent area, A^* , is defined as

$$A^* = \frac{c_d A_U A_L}{\left[\frac{1}{2} \left(\frac{c_d^2}{c} A_U^2 + A_L^2 \right) \right]^{1/2}}, \quad (52)$$

where c is the inlet loss coefficient and c_d is the discharge loss coefficient. Because the only interfacial transport is through the plume,

$$Q_v = Q(z = h). \quad (53)$$

Meanwhile, buoyancy conservation requires that

$$g'_u = g'(z = h) = F/Q. \quad (54)$$

From (51)–(54), we reproduce a result akin to (2.11) of Linden *et al.* [3],

$$\frac{A^*}{H^2} = \left(C \frac{Q}{Q_{(n=1)}} \right)^{3/2} \left(\frac{\zeta^5}{1 - \zeta} \right)^{1/2}, \quad (55)$$

where $\zeta = h/H$ is the nondimensional interface height and $Q_{(n=1)} = CF^{1/3} h^{5/3}$ where $C = \frac{6}{5} \left(\frac{9}{10} \right)^{1/3} \pi^{2/3} \alpha^{4/3}$. Using $Q_{\text{eff}} = (Q/Q_{(n=1)})^{3/4}$, (55) can be rewritten as

$$\frac{A^*}{H^2} = (C Q_{\text{eff}}^{4/3})^{3/2} \left(\frac{\zeta^5}{1 - \zeta} \right)^{1/2}, \quad (56)$$

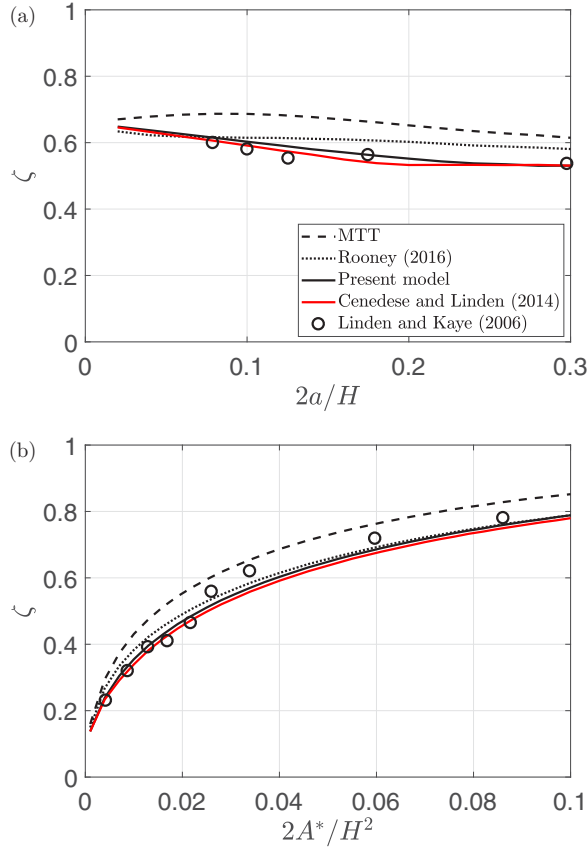


FIG. 11. Comparison of different model predictions with the experimental data of Linden and Kaye [12] for two merging plumes. (a) Interface height as a function of the distance from the plume source to the adjacent wall with $A^*/H^2 = 0.02$ (data reproduced from Fig. 8 of Linden and Kaye [12] with permission). (b) Interface height as a function of the effective vent area with $a/H = 0.05$ (data reproduced from Fig. 11 of Linden and Kaye [12] with permission).

on which basis we may define an effective constant, $C_{\text{eff}} = CQ_{\text{eff}}^{4/3}$ [21]. When $z = h$, ζ can be related to \hat{z} using $\zeta = \frac{\alpha^{-1}a}{H}\hat{z}$, which connects the theory in Sec. II to (56).

For $n = 2$, the flow illustrated in Fig. 10(b), the plume can be regarded as half of two merging plumes using the method of images. Linden and Kaye [12] performed laboratory experiments of two merging plumes with equal and unequal strengths in a ventilated enclosure. A comparison between the MTT, Rooney [15], the present model (27), Cenedese and Linden [13] (28), and the measured data of Linden and Kaye [12] is shown in Fig. 11. Here we focus on the steady-state interface height, ζ , and choose $\alpha = 0.13$ consistent with the classic MTT model. Good overall agreement between the present model and experimental measurements is observed.

For $n = 4$, which corresponds to a plume in a right-angle corner, Gao *et al.* [21] proposed a technique for computing the plume volume flux on the basis of the piecewise model of Cenedese and Linden [13] (28). Using the so-called principle of image theory, Gao *et al.* [21] argued that a plume in a right-angle corner is equivalent to the case of two plumes that share four times the effective vent area for a single room; see their Fig. 6. (Following the method of images strictly, the case of a plume in a right-angle corner is equivalent to four plumes with an effective vent area four times that of a single room). Mathematically, the governing equation for ζ , analogous to (56), is

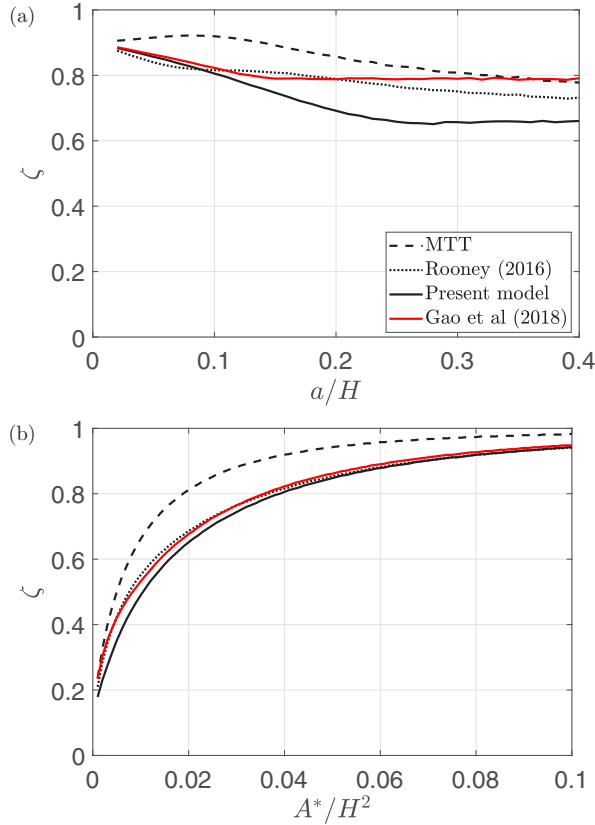


FIG. 12. Comparison of different model predictions for the ambient interface height ζ in the case of a plume in a right-angle corner. (a) Interface height as a function of a/H for $A^*/H^2 = 0.04$. (b) Interface height as a function of A^*/H^2 for $a/H = 0.1$. The red curve represents the solution of (57).

given by Gao *et al.* [21] as

$$\frac{2A^*}{H^2} = (CQ_{\text{eff, CL}}^{4/3})^{3/2} \left(\frac{\zeta^5}{1-\zeta} \right)^{1/2}, \quad (57)$$

where $Q_{\text{eff, CL}}$ is expressed by (28). A comparison of the MTT, Rooney [15], and present (27) models with the predictions of (57) is shown in Fig. 12, where we again focus attention on the interface height.² For relatively small a/H , (57) agrees satisfactorily with Rooney [15] and with (27); see Fig. 12(a). This agreement is also observed clearly in Fig. 12(b) wherein $a/H = 0.1$ is fixed. For larger a/H , entrainment is expected to be less influenced by the corner and the plume should therefore behave more like a free plume. In such cases, however, (57) approaches the solution for a free plume having twice the effective vent area of a single room, which overestimates the interface height compared to the predictions of Rooney [15] and (27). Among the different models, (27) predicts the lowest interface height when $a/H > 0.1$ [Fig. 12(a)]. This phenomenon is attributed to the fact that the present model does not underestimate entrainment especially in the near field; see

²Note that the difference between the red curve in Fig. 12(a) and the counterpart thick red curve in Fig. 7 of Gao *et al.* [21] is due to the smaller entrainment coefficient; $\alpha = 0.093$ listed in Table 1 of Gao *et al.* [21] is the entrainment coefficient assuming Gaussian rather than top-hat profiles.

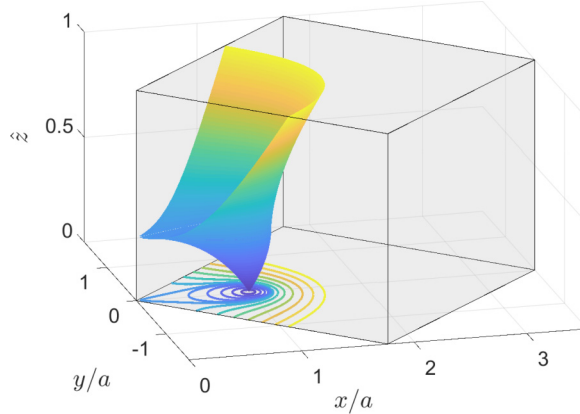


FIG. 13. Illustration of plume rise in a right-angle corner of a room (shaded gray). The plume boundaries are shaded according to the nondimensional height, and the contours are projected onto the bottom plane.

Fig. 5(b). For better visualizing plume rise in a right-angle corner, a three-dimensional contour plot using the present model (27) is illustrated in Fig. 13.

B. Non-Boussinesq plume

The non-Boussinesq plume theory described in Sec. IV is compared with experimental measurements of corner fire plumes by Takahashi *et al.* [27] whose configuration is shown in Fig. 14. Two different burner locations are considered with $S/D = 0.5$ and 2.0 . The distance between the burner center and the wall surface can be calculated by $a = S + D/2$ where $D = 0.1$ m. The heat release rate from the fire source is $\dot{Q}_c = 15$ kW. The buoyancy flux of the plume can be related to \dot{Q}_c by

$$F = \frac{g\dot{Q}_c}{c_p\rho_a T_a}, \quad (58)$$

where $c_p = 1006.1$ J/kg K is the air-specific heat capacity and $\rho_a = 1.2047$ kg/m³ is the air density at an ambient temperature $T_a = 293.15$ K. As inferred from Fig. 4 of Takahashi *et al.* [27], the fire

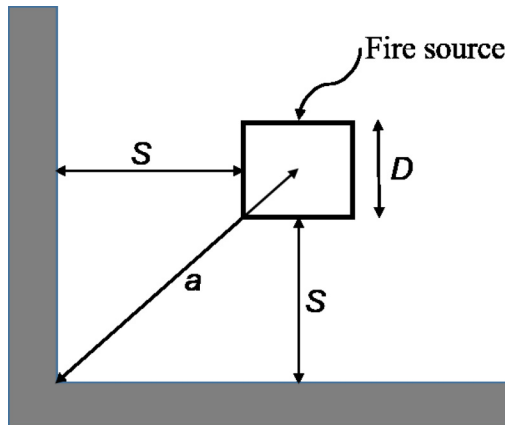


FIG. 14. Top view of a square ($D \times D$) fire source near a corner. The distance between the burner (i.e., fire source) edge and the wall surface is given by S , whereas a denotes the distance between the burner center and the corner vertex [27].

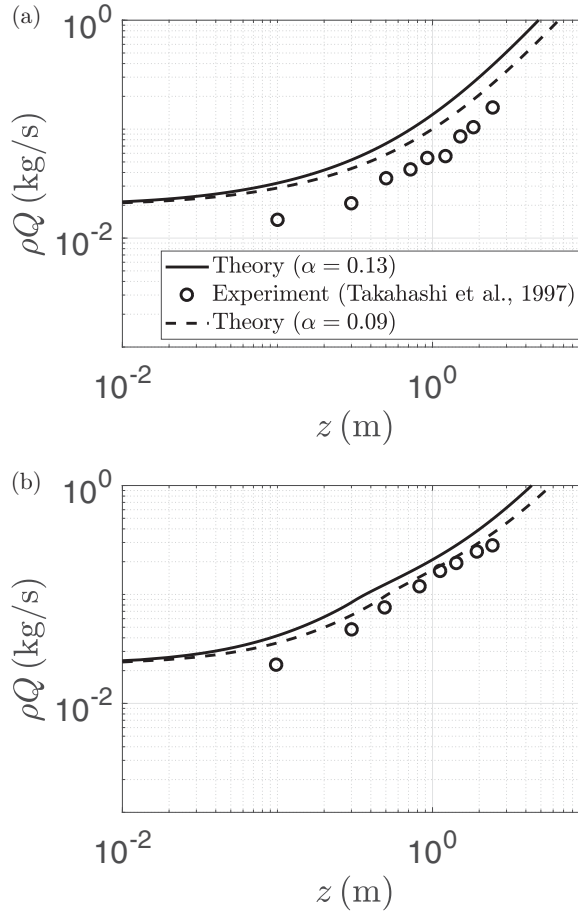


FIG. 15. Comparison of theory vs experiment in terms of mass flux at different heights for $S/D = 0.5$ (a) and 2 (b). The configuration is a fire in a right-angle corner as shown in Fig. 14.

source excess temperatures $T_0 - T_a$ for $S/D = 0.5$ and 2 are 743.1 K and 657.5 K, respectively. Thus following the ideal gas law, the source density ratio can be computed from $\eta_0 = \rho_0/\rho_a = T_a/T_0$. The source area is $A_0 = D^2$ and the nondimensional counterpart is $\hat{A}_0 = A_0/a^2$. Using $F = A_0 w_0 g(1 - \eta_0)$, the plume source velocity w_0 can be determined. With all the input parameters to the non-Boussinesq plume theory in hand, we compare the mass flux (ρQ) as a function of height (z) for theory versus experiment in Fig. 15. The theoretical model does not describe the flame region explicitly, however, the respective flame tip heights for the cases $S/D = 0.5$ and 2 are 0.73 m ($7.3D$) and 0.58 m ($5.8D$). The greater flame tip height for $S/D = 0.5$ is due to the more restricted mixing between the fuel and the ambient air.

The agreement between theory and experiment shown in Fig. 15 is satisfactory, given that the flame tip height is non-negligible compared to the maximum height of measurement. In general, using a smaller entrainment coefficient, $\alpha = 0.09$, slightly improves the agreement. Note also that the agreement for the case of $S/D = 2$ is better than that for $S/D = 0.5$. There are two explanations for this observation. First, and as noted above, the flame region is greater for $S/D = 0.5$. Second, the nonideal source effect for $S/D = 0.5$ is more pronounced, which renders the irrotational flow theory (i.e., assuming an ideal sink; see Sec. II A) less accurate in this small S/D case.

C. Boussinesq versus non-Boussinesq ventilation

A final point of interest concerns a comparison of Boussinesq versus non-Boussinesq plumes in a corner within a naturally ventilated enclosure. From the results presented in Sec. IV D, the non-Boussinesq height for a small source fire plume is expected to be negligible compared to the interface height within the ventilated room. Therefore, the difference between Boussinesq versus non-Boussinesq ventilation in the case of a “small fire” is expected to be small. As discussed in Sec. IV D 2, and when the nonideal source effect is important, e.g., the fire source is against the corner ($S/D = 0$ in Fig. 14), the difference between Boussinesq and non-Boussinesq plumes can be nontrivial. For the $S/D = 0$ case in Takahashi *et al.* [27], our theory predicts that the non-Boussinesq height is approximately 90% of the room height (3 m). This value will increase still further if the burner heat release rate increases such that the temperature of the hot layer below the ceiling also increases, possibly leading to flashover [26]. For this case, the flame region extends over nearly half of the room height and laminarization of the plume flow along the walls occurs [27]. In such scenarios, more work is needed to account for the flame region and the wall drag acting on the plume.

VI. CONCLUSIONS

The present study extends the models of Rooney [14,15] to describe Boussinesq and non-Boussinesq plume rise in a corner of arbitrary angle. We demonstrate that the complex potential (2), originally derived for n line sinks arranged equally around a circle, is able to describe a plume in a corner of angle $2\pi/n$, where n can be any real number satisfying $n \geq 1$. For noninteger n , theoretical solutions of the plume vertical velocity and volume flux approach their respective near- and far-field similarity limits as exhibited graphically in Figs. 2(a) and 2(b). Another finding of the present study is that the alternate entrainment assumption (27) yields good agreement with the model of Cenedese and Linden [13] in terms of the effective entrainment for the $n = 2$ case, i.e., a plume near a wall. To wit, the alternate entrainment assumption does not reduce entrainment in the near-field, depressed entrainment being a key limitation of previous entrainment formulations [15,18]. Moreover, this alternate entrainment assumption is simpler in that it does not introduce any empirical correlation for the entrainment coefficient. The application of the present model to naturally ventilated spaces yields good agreement with the experimental data of Linden and Kaye [12] *vis-à-vis* the interface height for the $n = 2$ case. For the $n = 4$ case, i.e., a plume in a right-angle corner, a comparison between different models shows that the present model predicts lower ambient interface heights than do previous models, this provided that the plume source is not too close to the corner.

Another major contribution of the present work is to extend the model of Rooney [15] to describe non-Boussinesq plume rise in a corner. We reveal that the plume vertical velocity and volume flux also approach their respective near- and far-field similarity solutions in the case of a non-Boussinesq source. For small source non-Boussinesq plumes, we find that the height over which non-Boussinesq effects are significant is negligible compared to the contact height between the plume and the corner (Figs. 6 and 7). For relatively large source plumes, we reveal that the non-Boussinesq height is comparable to the first contact height between the plume and the corner (Fig. 9). Moreover, non-Boussinesq effects are more pronounced for smaller corner angles. The theory of a non-Boussinesq plume in a corner compares satisfactorily with previous measurements, due to Takahashi *et al.* [27], of fire plume mass flux with height, although the theory does not account for the flame region. We note that when the nonideal fire source is situated just against the corner, theoretical results show that the non-Boussinesq effect persists over a nontrivial height, which may significantly enhance the likelihood of flashover.

A major limitation of the present study is that there are limited experimental data available for validation. Nonetheless, this study opens the door for several future endeavors. A topic of interest is to study the transient behavior of a naturally ventilated room forced by a plume in a corner. In

such a configuration, the critical value for A^*/H^2 beyond which the buoyant upper layer overshoots its steady-state height may be different from that anticipated for a centrally located plume [7]. It may also be interesting to investigate the behavior of a turbulent fountain in a corner. An isolated turbulent fountain in a uniform ambient consists of an inner jetlike upflow and an outer plume-like downflow. With the presence of a nearby corner, either the upflow or the downflow will first touch the corner surface whereafter the flow dynamics are expected to be significantly altered.

ACKNOWLEDGMENTS

Financial support was generously provided by Natural Sciences and Engineering Research of Canada (NSERC, Grant No. CRDJ 501081-16). We wish to thank Dr. Paul F. Linden and Dr. Nigel B. Kaye for sharing their experimental data for the purposes of model validation.

-
- [1] B. R. Morton, G. I. Taylor, and J. S. Turner, Turbulent gravitational convection from maintained and instantaneous sources, *Proc. R. Soc. London Ser. A* **234**, 1 (1956).
 - [2] W. Baines and J. Turner, Turbulent buoyant convection from a source in a confined region, *J. Fluid Mech.* **37**, 51 (1969).
 - [3] P. F. Linden, G. Lane-Serff, and D. Smeed, Emptying filling boxes: The fluid mechanics of natural ventilation, *J. Fluid Mech.* **212**, 309 (1990).
 - [4] G. C. Da Graça, P. F. Linden, and M. Brook, Design of the natural ventilation system for the new San Diego Children’s Museum, in *Proceedings of the Ninth international IBPSA conference, Montreal—Canada* (Energy Technologies Area, Berkeley Lab., 2005) pp. 349–356.
 - [5] P. F. Linden, The fluid mechanics of natural ventilation, *Annu. Rev. Fluid Mech.* **31**, 201 (1999).
 - [6] G. R. Hunt and P. F. Linden, The fluid mechanics of natural ventilation—Displacement ventilation by buoyancy-driven flows assisted by wind, *Build. Environ.* **34**, 707 (1999).
 - [7] N. B. Kaye and G. R. Hunt, Time-dependent flows in an emptying filling box, *J. Fluid Mech.* **520**, 135 (2004).
 - [8] G. Rooney and P. Linden, Strongly buoyant plume similarity and ‘small-fire’ ventilation, *Fire Safety J.* **29**, 235 (1997).
 - [9] D. G. Madival, Filling of smoke due to fire in a room with roof ventilation, *Int. J. Therm. Sci.* **160**, 106650 (2021).
 - [10] R. Akhter and N. B. Kaye, Experimental investigation of a line plume in a filling box, *Environ. Fluid Mech.* **20**, 1579 (2020).
 - [11] N. Kaye and P. F. Linden, Coalescing axisymmetric turbulent plumes, *J. Fluid Mech.* **502**, 41 (2004).
 - [12] P. F. Linden and N. B. Kaye, Interacting turbulent plumes in a naturally ventilated enclosure, *Int. J. Vent.* **4**, 301 (2006).
 - [13] C. Cenedese and P. F. Linden, Entrainment in two coalescing axisymmetric turbulent plumes, *J. Fluid Mech.* **752** (2014).
 - [14] G. G. Rooney, Merging of a row of plumes or jets with an application to plume rise in a channel, *J. Fluid Mech.* **771** (2015).
 - [15] G. G. Rooney, Merging of two or more plumes arranged around a circle, *J. Fluid Mech.* **796**, 712 (2016).
 - [16] Z. He and Y. Lou, Integral model for multiple forced plumes arranged around a circle in a linearly stratified environment, *Phys. Rev. Fluids* **4**, 123501 (2019).
 - [17] Y. Lou, Z. He, H. Jiang, and X. Han, Numerical simulation of two coalescing turbulent forced plumes in linearly stratified fluids, *Phys. Fluids* **31**, 037111 (2019).
 - [18] S. Li and M. R. Flynn, Merging of two plumes from area sources with applications to cooling towers, *Phys. Rev. Fluids* **5**, 054502 (2020).
 - [19] S. Li and M. R. Flynn, Merging of long rows of plumes: Crosswinds, multiple rows, and applications to cooling towers, *Phys. Rev. Fluids* **5**, 094502 (2020).

- [20] X. Gao, A. Li, and C. Yang, Study on thermal stratification of an enclosure containing two interacting turbulent buoyant plumes of equal strength, *Build. Environ.* **141**, 236 (2018).
- [21] X. Gao, A. Li, and C. Yang, Study on natural ventilation driven by a restricted turbulent buoyant plume in an enclosure, *Energy Build.* **177**, 173 (2018).
- [22] P. Cooper and G. R. Hunt, The ventilated filling box containing a vertically distributed source of buoyancy, *J. Fluid Mech.* **646**, 39 (2010).
- [23] N. Kaye and P. Cooper, Source and boundary condition effects on unconfined and confined vertically distributed turbulent plumes, *J. Fluid Mech.* **850**, 1032 (2018).
- [24] D. Parker, H. Burrige, J. Partridge, and P. Linden, A comparison of entrainment in turbulent line plumes adjacent to and distant from a vertical wall, *J. Fluid Mech.* **882**, A4 (2020).
- [25] E. Ezhova, C. Cenedese, and L. Brandt, Dynamics of three-dimensional turbulent wall plumes and implications for estimates of submarine glacier melting, *J. Phys. Oceanogr.* **48**, 1941 (2018).
- [26] F. W. Mowrer and R. B. Williamson, Estimating room temperatures from fires along walls and in corners, *Fire Technol.* **23**, 133 (1987).
- [27] W. Takahashi, O. Sugawa, H. Tanaka, and M. Ohtake, Flame and plume behavior in and near a corner of walls, *Fire Safety Sci.* **5**, 261 (1997).
- [28] K. McGrattan and D. Stroup, Wall and corner effects on fire plumes as a function of offset distance, *Fire Technol.* **57**, 977 (2020).
- [29] J. S. Turner, *Buoyancy Effects in Fluids* (Cambridge University Press, Cambridge, 1973).
- [30] B. Morton and J. Middleton, Scale diagrams for forced plumes, *J. Fluid Mech.* **58**, 165 (1973).
- [31] G. G. Rooney and P. F. Linden, Similarity considerations for non-Boussinesq plumes in an unstratified environment, *J. Fluid Mech.* **318**, 237 (1996).
- [32] P. Carlotti and G. R. Hunt, Analytical solutions for turbulent non-Boussinesq plumes, *J. Fluid Mech.* **538**, 343 (2005).
- [33] A. W. Woods, A note on non-Boussinesq plumes in an incompressible stratified environment, *J. Fluid Mech.* **345**, 347 (1997).